

Chiral nature of current flow in the regime of the quantized Hall effect

Serkan Sirt,¹ Matthias Kamm,¹ Vladimir Y. Umansky,² and Stefan Ludwig^{1,*}

¹Paul-Drude-Institut für Festkörperelektronik, Leibniz-Institut im Forschungsverbund Berlin e.V., Hausvogteiplatz 5-7, 10117 Berlin, Germany

²Weizmann Institute of Science, Rehovot 76100, Israel

The integer quantum Hall effect (QHE) belongs to the most fundamental phenomena of solid state physics and has an important application as resistance standard. It serves as a basis to understand the fractional, anomalous or spin QHEs, candidates for applications in quantum technology due to their topological properties. For optimizing all these applications it is essential to understand the current distribution inside the Hall bar, a question disputed for decades. We perform multiterminal current measurements on a Hall bar and compare the results with limiting models. We show, based on these simple experiments, that the current flow is chiral for the plateaus of quantized Hall resistance. Everywhere else, the current is described by the Drude model.

I. INTRODUCTION

Magnetic field is an axial vector and, therefore, breaks time-reversal symmetry, which, however, can be restored by the simultaneous reversal of magnetic field and time, $\vec{B} \rightarrow -\vec{B}$ and $t \rightarrow -t$. This property gives rise to the chiral trajectory of a free charged particle in a homogeneous magnetic field, the mirror symmetry of the current in a two-terminal measurement, $I(\vec{B}) = I(-\vec{B})$, or the point symmetry of the Hall voltage, $V_H(\vec{B}) = -V_H(-\vec{B})$. In this article, we explore the implication of the axial symmetry of \vec{B} for the current flow in the regime of the quantized Hall effect.

In the classical equation of motion, $m\dot{\vec{v}} = -e\vec{E} + \vec{F}_L$, the axial character of \vec{B} is expressed in terms of the vector product of the Lorentz force $\vec{F}_L = -e\vec{v} \times \vec{B}$ acting on an electron with charge $-e$ and effective mass m at the momentary velocity \vec{v} , exposed to the fields \vec{E} and \vec{B} .

The solution for a *ballistic electron* is an in-plane spiral-shaped trajectory composed of a uniform drift velocity $\vec{v}_d = \vec{E} \times \vec{B}/B^2 \neq \vec{v}$ and a cyclotron motion with radius $R_c = |\vec{v}|/\omega_c$, where $\omega_c = eB/m$ is the cyclotron frequency, cf. Fig. 1(a). If we define the chirality of a trajectory in analogy to the handedness of a screw thread, the above trajectory of a ballistic electron is left-handed (and would be right handed for a positive charge).

The Drude model describes magnetotransport in the classical limit of the *diffusive regime*. Its key parameter is the electron mobility μ . For $\mu B \lesssim 1$ (corresponding to a mean-free path $l_m \lesssim R_c$), the cyclotron motion is impeded by Markovian momentum scattering. Consequently, the Drude model neglects the cyclotron motion by assuming $\vec{v} = \vec{v}_d$. Applying the relaxation ansatz $\dot{\vec{v}}_d = \vec{v}_d/\tau$ with the momentum scattering time $\tau = m\mu/e$, the solution of the equation of motion introduced above in the diffusive limit becomes

$$\vec{v}_d = \frac{-\mu}{1 + (\mu B)^2} \left(\vec{E} - \vec{E} \times \mu \vec{B} \right) \text{ for } \vec{B} \perp \vec{E}. \quad (1)$$

[For $\vec{B} \not\perp \vec{E}$ there would be a third summand inside the parentheses, namely $\mu^2(\vec{E} \cdot \vec{B})\vec{B}$.] For finite B , \vec{j} is bent by the Hall

angle $\varphi = \angle(\vec{j}, \vec{E}) = \tan^{-1}(\mu B)$ in respect to \vec{E} , cf. Fig. 1(b). Importantly, as long as both the carrier density n_s and the mobility μ are homogeneous, the current density $\vec{j} = -en_s\vec{v}_d$ is homogeneous, too.

While the Drude model is designed to describe the limit of $\mu B \lesssim 1$, its prediction for the drift velocity for $\mu B \rightarrow \infty$ where the friction forces in Eq. (1) become negligible, namely $\vec{v}_d \rightarrow \vec{E} \times \vec{B}/B^2$, is identical to the ballistic solution. Since for $\mu B \rightarrow \infty$ the rapid cyclotron motion averages out over reasonable length scales, both models predict identical current densities, too, for $\mu B \rightarrow \infty$.

In the remainder of the article, we restrict ourselves to a two-dimensional electron system (2DES), which defines the xy -plane, with an in-plane electric field $\vec{E} = (E_x, E_y, 0)$ and a perpendicular homogeneous magnetic field $\vec{B} = (0, 0, B)$. This is a common scenario realized in many mesoscopic magnetotransport measurements.

To discuss the *classical limit of the Hall effect*, we include two sample edges at $y = 0$ and $y = b$, such that the electrons are confined in the y -direction but move freely in the x -direction, cf. Fig. 1(c). In the steady state, we expect $j_y = 0$ everywhere even for $B \neq 0$, because the edges reflect electrons. Applied to Eq. (1) $j_y = 0$ yields $E_y = -\mu B E_x$ and $j_x = E_y/R_H$ with the Hall resistance defined as $R_H = -\frac{B}{n_s e}$. Physically, the transversal field E_y is sourced by charge accumulated at the sample edges. With $E_y = \vec{\nabla} V_H$ it also gives rise to the Hall voltage V_H , that can be measured across the Hall bar. Because in steady state, the Lorentz force, acting on the carriers, is exactly canceled by $-eE_y$ (the forces associated with B and E_y cancel each other), inside the Hall bar the electrons move as if only the longitudinal electric field E_x was applied. Given a homogeneous sample (homogeneous distributions of n_s and μ away from the edges of the Hall bar), the current density j_x is uniform and the current is $I = j_x b$, with b being the width of the Hall bar.

While the Drude model predicts a homogeneous current density for the classical Hall effect, the axial character of the magnetic field and the breaking of the time-reversal symmetry are manifest in the edge charges and the related Hall voltage. In addition, the Hall resistance is non-local as it does not cause any dissipation inside the Hall bar: At $B = 0$ the two terminal current measurement of a Hall bar is the sum of the ohmic sample resistance and the resistance of the leads (including the ohmic contacts), $R_{2T}(0) = R_0 + R_{\text{leads}}$. At finite

* ludwig@pdi-berlin.de

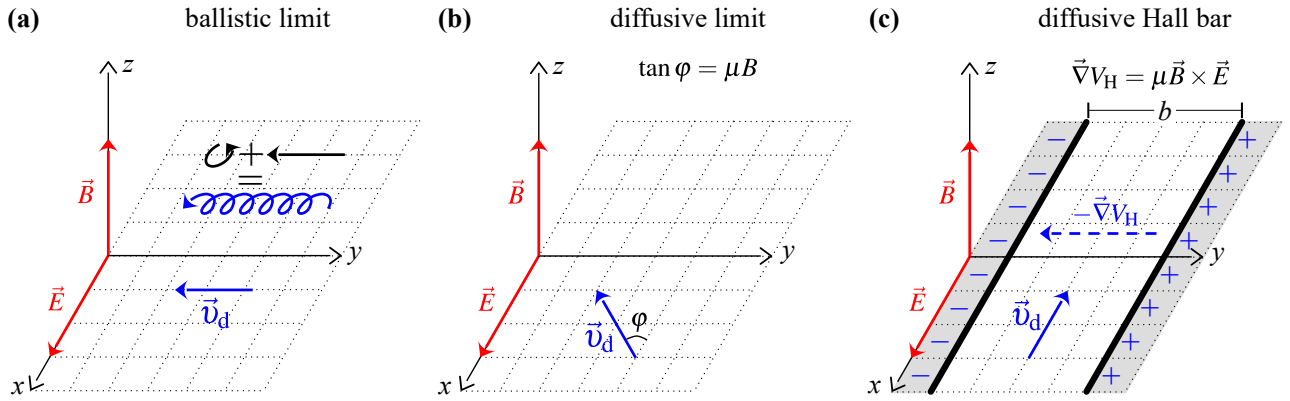


FIG. 1. Motion (expressed by drift velocity) of an electron confined to the xy -plane with in-plane electric and perpendicular magnetic fields, \vec{E} and \vec{B} (red arrows), respectively. (a) Ballistic limit (free electron). The spiral is the classical trajectory consisting of a uniform drift velocity $\vec{v}_d = \vec{E} \times \vec{B}/B^2$ and a (left-handed) cyclotron motion with its radius being proportional to the initial velocity. (b) Diffusive limit. For $|\mu B| < 1$ the spiral motion is damped. However, the magnetic field reduces the drift velocity by the factor $1/\sqrt{1 + (\mu B)^2}$ and tilts it by the Hall angle ϕ . (c) Diffusive Hall bar in the steady state limit with edges parallel to the applied \vec{E} (red arrow). The Hall voltage compensates the Lorentz force, $-e\vec{\nabla}V_H = \vec{F}_L$ (or $E_y = |\vec{F}_L|/e$), such that the drift velocity is \vec{v}_d as for $\vec{B} = 0$.

B , the non-local Hall resistance enhances the resistance of the Hall bar, such that $R_{2T}(B) = \sqrt{R_0^2 + R_H^2} + R_{\text{leads}}$.

As we increase B , at low enough temperatures the quantization of the density of states into discrete Landau-levels results in the *quantum Hall effect* (QHE). Its main features are plateaus of quantized Hall resistance accompanied by a vanishing longitudinal resistance ($R_0 = 0$). The latter indicates the absence of momentum scattering within the Hall bar for a quantized Hall resistance, in agreement with the classical Drude prediction for $\mu B \rightarrow \infty$.

To explain the quantized values of R_H , the Landauer-Büttiker picture (LBP) assumes the formation of chiral, one-dimensional (1D) edge channels, such that backward scattering is suppressed [1, 2]. The conductance of a spin-resolved 1D channel without momentum scattering is e^2/h , which concurs with the observed quantization of the Hall resistance, $R_H = R_K/\nu$, in fractions of the von-Klitzing constant $R_K = h/e^2$. The filling factor ν describes the number of edge channels and is equal to two-times the filling fraction of the (spin-degenerate) Landau levels in the 2D bulk. The LBP assumes that the edge channels form where the potential energy of the Landau levels, which increase towards the depleted sample edges, intersect with the Fermi level [1, 2]. To obtain finite ranges of quantized Hall resistances, additionally the bulk (between the edge channels) is assumed to be insulating due to Anderson localization. The direction of the current flow in the edge channels is predetermined by the gradient of the confinement potential. This yields chiral current flow, more precisely, current flow in opposite directions along opposite edges.

The LBP provides an intuitive explanation for the quantized Hall resistance and the vanishing longitudinal resistance of the QHE. While its merit is its simplicity, its predictions are limited due to the phenomenological character as well as its neglect of interactions and non-equilibrium effects. In particular, the single particle assumption of the LBP leads to the prediction of a stepwise increase of the carrier density at the

edges of the Hall bar because of the successive population of Landau levels [3, 4]. Hence, neglecting the Coulomb interaction between carriers in the LBP causes the formation of highly charged stripes between the edge channels. This local polarization corresponds to an unrealistically large Coulomb energy. Another weak point of the LBP is the coexistence of occupied and unoccupied states inside the current carrying edge channels at the chemical potential. Even, if we assume chiral edge channels, an almost complete suppression of carrier scattering, as indicated by the accuracy of the measurements of the von Klitzing constant, is unlikely under any realistic conditions.

The screening theory [3–9] offers an alternative explanation of the highly accurate resistance values in fractions of h/e^2 . By taking into account the direct Coulomb interaction between electrons, it overcomes the limitations of the LBP. The Coulomb interaction causes a rearrangement of the free carriers such that the highly charged stripes are avoided. Early purely classical formulations considered this screening based on the Thomas-Fermi approximation [3, 4]. They demonstrated that the Landau-quantization leads to a segmentation of the 2DES of a Hall bar in compressible regions and incompressible strips (ICSs). The term ICS denotes areas of the 2DES, where the chemical potential lies within a local energy gap between completely filled and empty Landau levels. For this reason, at low enough temperature, inside the ICSs carriers cannot scatter and screening of the electric field is absent. ICSs are accompanied by adjacent compressible regions, in which a partly filled Landau-level is aligned with the chemical potential. Hence, inside compressible regions, carriers can scatter. Provided the vicinity of unscreened ICSs, the screening of the local electric field becomes perfect inside the compressible regions. The early calculations already show, that both, width and position of the ICSs depend on the magnetic field as well as the local electron density distribution $n_s(x, y)$ at $B = 0$. Later, for given boundary condi-

tions the number and geometry of the ICSs were predicted more accurately using a self-consistent numerical calculation of Poisson's equation within the Thomas-Fermi approximation and accounting for the quantum mechanical wavefunctions of the electrons in a mean field approach [7–9] (later confirmed in a full self-consistent approach of the quantum-electrostatic problem [10]). The calculations predict, that towards the higher magnetic field end of each plateau the ICSs merge into a single extended incompressible region centered in the Hall bar [7–9]. These predictions clearly confirmed the electrostatic landscape measured in scanning probe spectroscopy experiments as a function of the magnetic field [11–13].

According to the screening theory the electric field vanishes inside the perfectly screened compressible regions while it is exclusively contained inside the ICSs. For suppressed scattering the drift velocity of the electrons is $\vec{v}_d = \vec{E} \times \vec{B}/B^2$. Hence, the current density, $\vec{j} = -en_s \vec{v}_d$, vanishes in the compressible regions, while all current flows inside the ICSs [4, 9, 14, 15]. In case of a bulk ICS, current should then flow in the center of the Hall bar. Recently, we confirmed the predicted bulk current directly by means of an additional tiny ohmic contact in the center of a Hall bar [16]. Both, the electrostatics and the existence of bulk currents, predicted by the screening theory [9] and confirmed in measurements [11–13, 16] are in direct contrast to the assumptions of the LBP. Therefore, it is important to find out, whether another assumption of the LBP, which is often used, remains correct, namely whether the current flow is chiral for the quantized plateaus of the Hall resistance.

Even within the screening theory this is still a controversial question [3, 4, 9, 10, 15]. In the present article, we explore the question of chirality experimentally by employing multi-terminal current measurements. Thereby, we probe the division of the current into various ohmic contacts of the Hall bar. Clearly, we do not directly probe the local current density distribution. Nevertheless, it is possible to distinguish between chiral versus non-chiral transport as the current division into multiple contacts directly depends on it. To quantify this dependence, we use the properties of the macroscopic scattering matrix, which yields the division of the current into various contacts as follows: In the case of chiral current flow, only unidirectional transmission coefficients connecting adjacent contacts are non-zero. In comparison, non-chiral current flow requires additional non-zero transmission coefficients, which would ultimately yield a different division of the current into the various contacts.

Here, we show that the measured current division can be described for arbitrary magnetic fields by either one of two limiting models, introduced in Sec. II below. In Sec. III, we then present our three- and four-terminal current experiments, compare them with the predictions of the two limiting models and discuss our results.

II. MODELS

Our first model generically assumes coherent and chiral current flow. The condition of coherence is technical. In prac-

tice, it is sufficient to assume the absence of scattering. The second model applies the classical Drude model to a multi-terminal current measurement. It describes diffusive and non-chiral current.

Our experiments in Sec. III show, that the generic chiral model applies for the magnetic field regions of the plateaus of quantized Hall resistance, while the Drude model describes the situation for all other magnetic fields.

A. Coherent and chiral model of n -terminal device

Our first model describes the limit of coherent and chiral current flow inside the 2DES of a sample equipped with n ohmic contacts, cf. Fig. 2. The inner circle in Fig. 2 in-

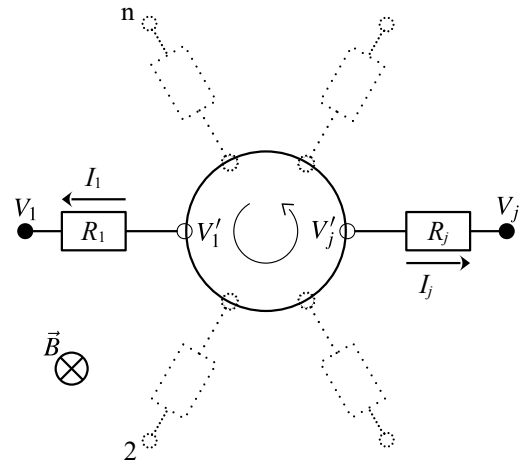


FIG. 2. Simplified circuit diagram of an n -terminal device. The inner circle indicates coherent and chiral current flow inside the 2DES. Each contact $i = 1, \dots, n$ has an ohmic resistance R_i and a voltage V_i applied in respect to the electrical ground. V'_i are the voltages resulting at the intersections between the ohmic contacts and the coherent inner circle. The magnetic field vector pointing into the plane of the 2DES gives rise to a right handed chirality of a free charge which translates into a left handed chirality of the device, cf. circled arrow.

icates the 2DES, the radial lines symbolize the n terminals $i = 1, 2, \dots, n$ connected via ohmic contacts to the 2DES. External voltages V_i can be applied to the contacts in respect to ground, while $V'_i = V_i + I_i R_i$ are the voltages present at the intersects of the 2DES and each contact. The current I_i flows through the i th contact via the ohmic resistance R_i to ground.

To describe the current flow through the 2DES (inner part of the sample), we employ the Landauer-Büttiker formalism (not to be confused with the LBP) and write

$$I_i = \sum_{j=1}^n G_{ij} V'_j = (V'_i - V_i)/R_i, \quad (2)$$

where G_{ij} are the conductance coefficients between mutual contacts. They can be formally derived from the scattering matrix of the problem. The left hand side of Eq. (2) is a general formulation of the transmission properties of the 2DES

based on the Landauer-Büttiker formalism, while the last term of Eq. (2) applies Ohm's law to the macroscopic contacts. If the transport within the 2DES is chiral, only those $G_{i,j \neq i}$ connecting adjacent contacts can be non-zero. The direction of the chirality is linked to the direction of the magnetic field vector. In our case sketched in Fig. 2, we consider \vec{B} pointing into the plane of the 2DES, such that $G_{ij} \neq 0$ for $i = j + 1$. Assuming coherent transport, the scattering matrix is unitary, implying $\sum_i G_{ij} = \sum_j G_{ij} = 0$, such that our coherent and chiral conductivity tensor takes the form

$$G_{ij} = \nu G_0 \begin{cases} 1; & i = j + 1 \\ -1; & i = j \\ 0; & \text{else} \end{cases}, \quad (3)$$

where $G_0 = e^2/h$ and ν is the filling factor of the (spin-resolved) Landau-levels. While the assumption of coherence guaranties a unitary scattering matrix, for the validity of Eq. (3) it is actually sufficient to require the absence of momentum scattering. For the quantized plateaus of the Hall resistance ν is an integer. Inserting Eq. (3) into Eq. (2) yields a solvable linear equation system providing us with the prediction of the current into the i th contact

$$I_i = \frac{V'_i - V_i}{R_i} \quad \text{with} \quad V'_i = \frac{1}{P_i} \left(\frac{S_n}{P_n - 1} + S_i \right), \quad (4)$$

$$P_i = \begin{cases} \prod_{j=1}^i \left(1 + \frac{1}{\nu G_0 R_j} \right); & i = 1, 2, \dots, n \\ 1; & i = 0 \end{cases}$$

and

$$S_i = \sum_{j=1}^i P_{j-1} \frac{V_j}{\nu G_0 R_j}.$$

A simplifying special case of some relevance is that of $V_1 \neq 0$ but all other applied voltages $V_{i>1} = 0$, which yields the current ratios

$$\frac{I_{i>1}}{I_1} = \frac{P_n/P_i}{1 - P_n/P_1} \frac{1}{\nu G_0 R_i}.$$

B. Drude model of an n -terminal device

The Drude model provides a solution of Eq. (2), which describes the classical limit of diffusive and incoherent currents inside the 2DES. Using $\vec{j} = -en_s \vec{v}_d$ we can rewrite Eq. (1) in terms of the magnetic-field-dependent conductivity tensor as

$$\begin{pmatrix} j_x \\ j_y \end{pmatrix} = \frac{\sigma_0}{1 + (\mu B)^2} \begin{pmatrix} 1 & -\mu B \\ \mu B & 1 \end{pmatrix} \begin{pmatrix} E_x \\ E_y \end{pmatrix}, \quad (5)$$

where the specific conductivity (defined at $B = 0$) is $\sigma_0 = en_s \mu$. For a laterally confined 2DES, in the steady state we expect $j_y = 0$, which implies $E_y = -\mu B E_x$ and, consequently, $j_x = \sigma_0 E_x = R_H^{-1} E_y$.

The structure of the conductivity tensor allows us to partition the non-vanishing current density j_x into two components with distinct physical meanings, namely

$$j_x \equiv j_{xx} + j_{xy} \quad \text{with} \quad (6)$$

$$j_{xx} = \frac{\sigma_0}{1 + (\mu B)^2} E_x \quad \text{and} \quad j_{xy} = \frac{(\mu B)^2}{1 + (\mu B)^2} \frac{1}{R_H} E_y.$$

The longitudinal component $j_{xx} = \sigma_{xx} E_x$ is the ohmic term, proportional to the specific conductivity and driven by the longitudinal electric field E_x . Caused by the additional Hall resistance at finite B , the ohmic current density is reduced by the factor $[1 + (\mu B)^2]^{-1}$. The transversal component $j_{xy} = \sigma_{xy} E_y$ is driven by the perpendicular electric field and attenuated by the non-local Hall resistance. For $\mu B \gg 1$ the ohmic component j_{xx} vanishes and the current density $j \rightarrow j_{xy}$ becomes independent of σ_0 . It implies, that momentum scattering is absent. At the same time, the transversal j_{xy} is bent into a current carrying contact as it follows the charged edge of the Hall bar.

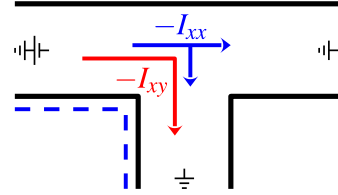


FIG. 3. Drude model: Simplifying sketch showing the partitioning of the current contributions I_{xx} versus I_{xy} at a three-terminal junction. A negative voltage is applied to the left contact, while the other contacts are grounded. I_{xx} is divided according to Kirchhoff's current rule. Neglecting the partial reflection of current at ohmic contacts, only one edge is negatively charged, other edges are at ground potential. I_{xy} is guided by the charged edge and flows entirely from the left to the lower contact.

In our experiments, we measure the current, which corresponds to the integral of the current densities in Eq. (6) across the Hall bar. For the partition of the current at a junction we can now use the following rules: The ohmic I_{xx} branches according to Kirchhoff's current law. For simplicity, we neglect the small resistance R_0 of the 2DES ($R_i/R_0 \sim 50$). The non-ohmic I_{xy} partitions according to Eq. (4), if we include non-integer filling factors [$R_H = (\nu G_0)^{-1}$]. Therefore, in the limit $\mu B \gg 1$, the prediction for the current division of the Drude model becomes identical to that of our coherent and chiral model derived in Sec. II A. To illustrate the different behaviors of I_{xx} and I_{xy} , in Fig. 3 we sketch the current division at a three-terminal junction. Combining both contributions, the Drude model predicts

$$I_i = I_{xx}^{(i)} + I_{xy}^{(i)} \quad \text{with}$$

$$I_{xx}^{(i)} = \frac{1}{1 + (\mu B)^2} \frac{1}{R_i} \left[\frac{\sum_{m=1}^n V_m/R_m}{\sum_{m=1}^n 1/R_m} - V_i \right] \quad (7)$$

$$I_{xy}^{(i)} = \frac{(\mu B)^2}{1 + (\mu B)^2} \frac{1}{R_i} \left[\frac{1}{P_i} \left(\frac{S_n}{P_n - 1} + S_i \right) - V_i \right]$$

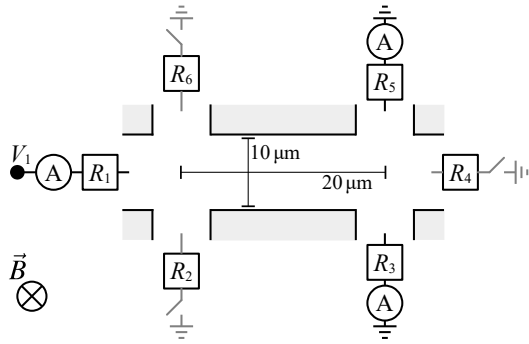


FIG. 4. Sketch of a Hall bar with six contacts, characterized by their ohmic resistances, R_i . We apply a voltage V_1 to contact 1 and measure currents into contacts 1, 3, and 5. Contacts 2, 4, and 6 can be left floating or connected to electrical ground. Current amplifiers at contacts 3 and 5 result in additional voltages of $\simeq 20\mu\text{V}$ applied to contacts 3 and 5 (not shown, but taken into account for generating model curves). \vec{B} points into the plane of the 2DES.

for the current flowing into the i th contact.

The original scope of the classical Drude model was a description of diffusive transport at $\mu B \lesssim 1$. Interestingly, in the limit $\mu B \rightarrow \infty$, the first term of Eq. (7) vanishes, $I_{xx} \rightarrow 0$, and the prediction of the Drude model becomes identical to Eq. (4). This property also means that for the limits $\mu B \lesssim 1$ versus $\mu B \gg 1$, Eq. (7) precisely describes both of our limiting models. For intermediate μB , Eq. (7) smoothly interpolates between the limits. This is useful, because $\mu(B)$ strongly oscillates due to the Shubnikov-de-Haas oscillations.

III. EXPERIMENTAL RESULTS AND DISCUSSION

Multiterminal current measurements yield the distribution of current into various contacts. In this section, we discuss the results of multi-terminal measurements and compare them with theory predictions in a wide magnetic field region corresponding to $1 \lesssim \nu < \infty$. We will see, that even though multi-terminal measurements do not provide the local current distribution across the Hall bar, their comparison with reasonable limiting models can provide answers to the questions about chirality of the current for the QHE.

A. Sample and measurement setup

We use a Hall bar as sketched in Fig. 4. It is etched from a GaAs/(Al,Ga)As heterostructure, which contains a two-dimensional electron system (2DES) 130 nm beneath the surface. We performed the experiments at a temperature of $T \simeq 300\text{mK}$ in a He-3 evaporation cryostat. At this temperature and zero magnetic field, the electron density and mobility of the 2DES, determined from Hall measurements, are $n_s \simeq 1.2 \times 10^{11} \text{ cm}^{-2}$ and $\mu \simeq 3.95 \times 10^6 \text{ cm}^2/\text{Vs}$ (yielding a mean-free-path of $\lambda_m \simeq 23 \mu\text{m}$), respectively.

For multi-terminal current measurements, we apply the

voltage of $V_1 = \pm 1 \text{ mV}$ to the source contact 1 (using a Keithley 2450 source meter). We measure the current $I_1(B)$ flowing from the Hall bar into contact 1, using the source meter, and the currents $I_3(B)$ and $I_5(B)$ flowing into contacts 3 or 5, respectively, using Basel Precision Instr. current amplifiers. Contacts 3 and 5 are connected to the electrical ground, while the remaining contacts 2, 4, and 6 may be either electrically floating or connected to ground depending on the experiment, cf. Fig. 4. Here, we apply B perpendicular to the 2DES, such that it points from the sample surface towards the 2DES, hence, electrons contributing to I_{xy} move from contact to contact along the counterclockwise pathway $1 \rightarrow 2 \rightarrow 3 \rightarrow 4 \rightarrow 5 \rightarrow 6 \rightarrow 1$. Due to the direction of the magnetic field and a voltage applied to contact 1, the largest portion of I_{xy} will always flow between contact 1 and contact 3, if contact 2 is floating, or to contact 2, if it is grounded. Whether this current is positive or negative depends on the sign of V_1 .

We performed a series of measurements at $B = 0$ to determine the contact resistances ($R_i \sim 2.5 \text{ k}\Omega$) and offset voltages ($V_{3,5} \sim 20 \mu\text{V}$) of the two current amplifiers. In addition, we used the comparison between measured data and model curves for a fine tuning of these circuit parameters, which remain constant between measurements. They are listed in Table I.

contact i	resistance R_i (Ω)	voltage V_i (mV)	geometry a_i
1	2420	1.000	1
2	2420	0	0.5
3	2400	-0.021	1
4	2350	0	1
5	2420	-0.018	1
6	2400	0	0.5

TABLE I. Parameters of the circuit sketched in Fig. 4. Contact resistances R_i include ohmic contacts, cables and RC -filters. Voltage V_1 is applied to contact 1, V_2 and V_3 are offset voltages of the current amplifiers. To account for the contribution of the Hall bar itself to the resistance, we defined a geometry parameter and use $R_i \rightarrow R_i + a_i/[n_s e \mu(B)]$ in the model calculations of the ohmic contributions. The correction is negligible for $B = 0$.

B. Three-terminal measurements

First, we discuss a three-terminal measurement in a mirror symmetric geometry, for which we keep the contacts 2, 4 and 6 electrically floating; current flows from contact 1 into contacts 3 and 5. In Fig. 5(a), we present as solid (blue) lines the measured current ratios $-I_3(B)/I_1(B)$ and $-I_5(B)/I_1(B)$. As expected, we find that $|I_3|$ increases with B while $|I_5|$ decreases accordingly, such that $I_3(B) + I_5(B) = -I_1(B)$. The dashed black line indicates the prediction of the model according to Eq. (7) for $n = 3$ if we assume a constant mobility $\mu(B) = \mu_0 \equiv \mu(B = 0) = 395 \text{ m}^2/\text{Vs}$. For this large mobility, the Ohmic term (first term) of Eq. (7) can be neglected for $B \gtrsim 50 \text{ mT}$ (corresponding to $\mu B \gtrsim 20$), such that with

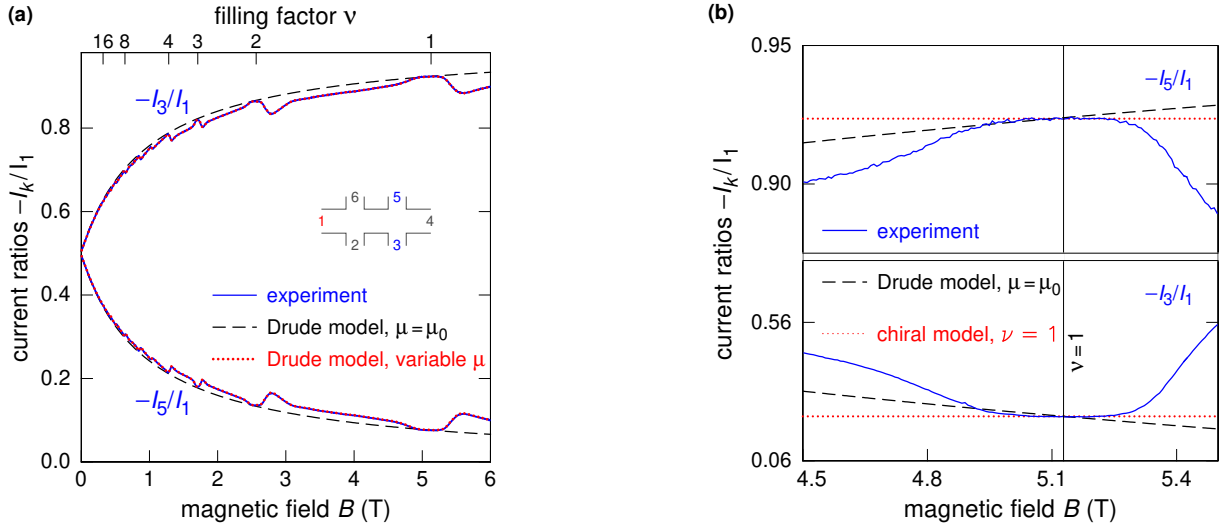


FIG. 5. Three-terminal measurement with symmetric circuit, cf. inset in (a). A voltage of $V = 1$ mV is applied to contact 1, while contacts 3 and 5 are connected to ground via current amplifiers; contacts 2, 4, and 6 are electrically floating. \vec{B} points from the surface into the 2DES plain such that I_{xy} is bent towards contacts 2 and 3. (a) Current ratios $-I_3/I_1$ and $-I_5/I_1$ as a function of magnetic field B (solid blue lines); Drude model prediction of Eq. (7) assuming constant $\mu = \mu_0$ (dashed black line); fit of Drude model prediction of Eq. (7) with $\mu(B)$ as free parameter (dotted red lines). (b) enlargements near $\nu = 1$ showing experimental data, the Drude model prediction for $\mu = \mu_0$ and the model prediction of Eq. (4) for coherent and chiral current at $\nu = 1$ (dotted red lines).

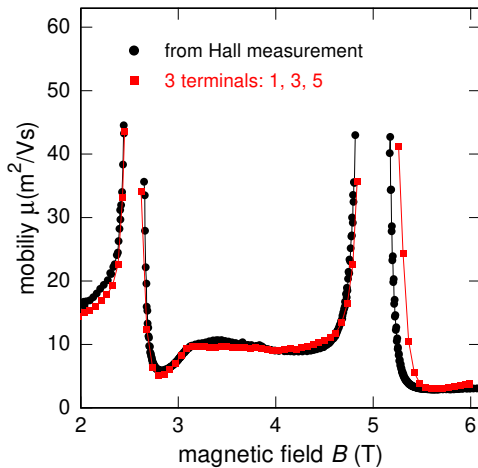


FIG. 6. Mobility $\mu(B)$ as determined from SdH-oscillations of the longitudinal resistance between contacts 2 and 3 (black dots) in comparison with $\mu(B)$ found by fitting Eq. (7) to the three-terminal measurements shown in Fig. 5 (red squares).

$(\nu G_0)^{-1} = R_H(B)$ Eq. (4) [Drude model] and Eq. (7) [chiral model] become identical.

In the classical limit for $B \lesssim 0.5$ T the Drude model agrees well with our measurement. As we increase B further, the Drude model still predicts the correct trend but as long as we use a constant $\mu(B) = \mu_0$ (black dashed lines), we observe growing deviations. These are clearly visible in the enlargement around the first plateau at $\nu = 1$ in Fig. 5(b). The red dashed lines are the prediction of the chiral model according

to Eq. (4) [or Eq. (7) using $\mu B = \infty$], where we inserted a constant filling factor $\nu = 1$. It perfectly fits the plateau values of the current ratios. An exact match between measurements and model beyond the plateaus can be achieved by using $\mu(B)$ as a free fit parameter in Eq. (7). For the dotted red line in Fig. 5(a), we used the magnetic field dependent values of $\mu(B)$ as shown by red squares in Fig. 6. For comparison, we have also determined $\mu(B)$ from the Shubnikov-de-Hass oscillations of a standard longitudinal resistance measurement, see the black dots in Fig. 6. [17] The general agreement between the $\mu(B)$ values obtained from longitudinal resistance measurements with those obtained by fitting Eq. (7) to our three-terminal current measurements supports the validity of our model.

The two regions of divergent $\mu(B)$ in Fig. 6 correspond to the plateau regions with the local filling factors $\nu = 2$ and $\nu = 1$. Here, I_{xx} vanishes. Away from the plateau regions, we find strongly reduced mobility values, indicating a transition to diffusive transport. The difference between the Drude model predictions for $\mu = \mu_0$ [dashed line in Fig. 5(a)] and the measured currents is the ohmic current contribution I_{xx} , which becomes clearly visible for $\mu < 20$.

So-far we have discussed three-terminal current measurements. With the knowledge of the contact resistances of our sample, we can quantitatively compare the experiments with model predictions. Between the plateaus, the mobility is reduced and the Drude model fits perfectly to our data, indicating non-chiral transport. Regarding the plateau regions, our three-terminal measurements are clearly consistent with chiral transport. Importantly, any additional non-zero transmission coefficients in Eq. (3) due to non-chiral currents would mod-

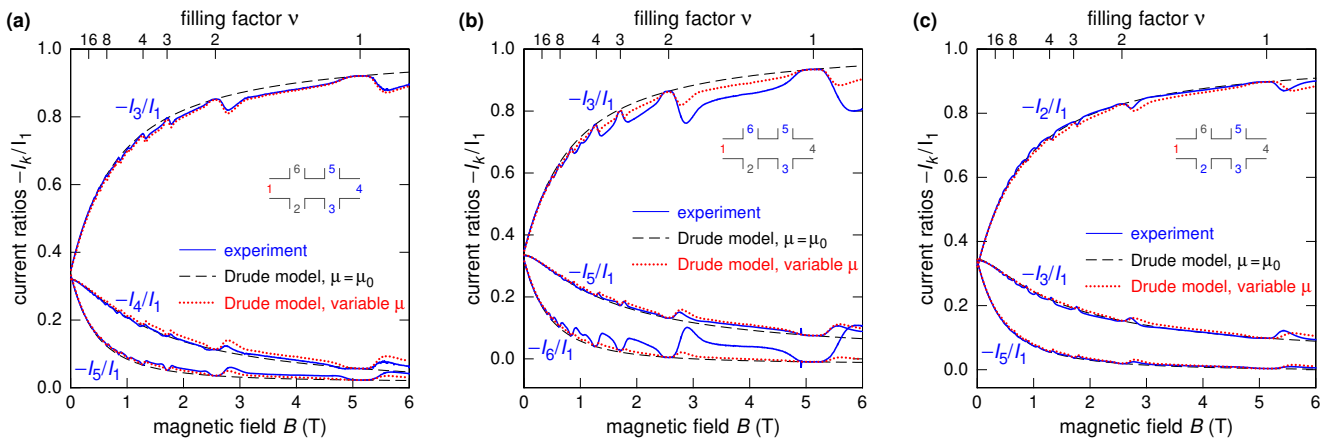


FIG. 7. Four-terminal measurements for three different contact configurations; the blue numbers in the insets indicate grounded contacts, black numbers indicate floating contacts and the external voltage is applied to contact 1 (red); further details as in Fig. 5; (a) symmetric four-terminal circuit; (b) and (c) asymmetric configurations.

ify the prediction of Eq. (4). Clearly, we do not observe such deviations.

C. Four-terminal measurements

In Fig. 7, we present current ratios $-I_i/I_1$ for three different four-terminal measurements (blue solid lines). Again, we measure the currents into contacts $i = 1, 3$ and 5, but now we ground an additional contact, namely contact 4 in Fig. 7(a), contact 6 in (b), and contact 2 in (c). If we assume $\mu(B) = \mu_0$, Eq. (7) reproduces the overall dependences $I_i(B)$ with a similar accuracy and similar deviations as it did for the three-terminal measurement (dashed black lines). The dotted red lines correspond to the predictions of Eq. (7), where we used the identical $\mu(B)$ that we found by fitting the three-terminal measurement above, cf. Fig. 6. As it was the case for the three terminal measurements, for the plateau regions, corresponding to diverging $\mu(B)$, the agreement between theory and the measured currents is perfect. However, away from the plateaus, the theory curves using the varying $\mu(B)$ does no longer yield a perfect agreement between theory and measured data. It means, that the division of the ohmic I_{xx} component of the current is not accurately predicted.

Nevertheless, our four-terminal measurements confirm the main conclusions of our three-terminal measurements: (1) Away from the plateaus, the transport is not chiral. (2) For the plateau regions, the agreement between our four-terminal measurements and the chiral and coherent model supports chiral transport.

D. Limits of our model in the diffusive regime

Away from the plateaus, the measured currents depend on the contact configuration beyond the predictions of our model. We conjecture, that our initial assumption of a homogeneous

Hall bar fails near the intersections. In the regime of diffusive transport it implies a homogeneous electric field inside the Hall bar. In reality, near intersections, both components, E_x and E_y , of the electric field and, therefore, the currents I_{xx} and I_{xy} become inhomogeneous. While I_{xy} is still completely bent into the contacts, the division of I_{xx} is influenced by its inhomogeneity. A more realistic model would require a suitable numerical calculation, e.g., based on a path integral formalism. We conjecture, that such a corrected model would yield perfect agreement with measurements, namely that the Drude model is still correct for more than three terminals, where it worked perfectly for three terminals.

E. Purely experimental confirmation of non-chiral currents between plateaus

In Fig. 8, we plot for each of the three four-terminal measurements shown in Fig. 7 only the branch I_k/I_1 corresponding to the largest current. In a chiral model, this is the current flowing into the first grounded contact after emission from contact 1. We slightly scaled the data (based on the values provided in Table I) to compensate for small variations in the contact resistances. After scaling, the three curves are identical in the classical regime ($B < 0.5T$) as well as on the plateaus of the QHE. The line linking shaded and white backgrounds corresponds to the prediction of Eq. (7) for constant $\mu = \mu_0$ [equal to the dashed black lines in Fig. 7(a)].

Compared to the model prediction, between the plateaus the current is reduced for all three geometries, which above we already interpreted in terms of a finite contribution of the non-chiral I_{xx} . Because the various contact resistances of our sample are almost identical, for a purely chiral current flow the branches of the largest current $I_k(B)/I_1$, shown in Fig. 8 should be independent of the details of the contacts configuration (as long as the overall number of grounded contacts remains the same). The fact that $I_k(B)/I_1$ varies between con-

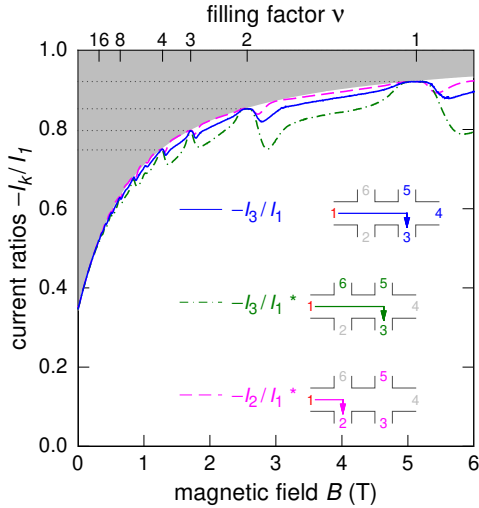


FIG. 8. Comparison of the respective largest measured current contributions flowing into a grounded contact for three different configurations of four-terminal measurements. The dotted horizontal lines depict the predicted current ratios for filling factors $1 \leq \nu \leq 4$. The current ratios I_i/I_1 marked with a * are slightly scaled to account for the slightly different contact resistances, such that all three theory curves according to Eq. (7) with $\mu = \mu_0$ are identical and follow the edge between shaded and white backgrounds. Sketches: Arrows indicate the displayed current branches; colored numbers indicate current carrying and gray numbers floated contacts.

figurations, is a direct experimental prove of non-chiral currents between the quantized plateaus.

This conclusion experts additional support by a closer look at the amounts of current reduction: It systematically depends on the relative distances between contact 1 and the grounded contacts on both sample edges in a way that contradicts chiral current flow.

F. Formulation of the proof of chiral current flow for quantized Hall resistance

So far, we have proven non-chiral current flow between the quantized plateaus, while for the quantized plateaus we have merely stated that our experimental results are consistent with chiral current flow. However, our analysis allows a stronger statement, namely that the agreement between the chiral model and our measurements is a prove of chiral current flow.

The proof is based on the coherent and chiral model introduced in Sec. II A. Based on the Landauer-Büttiker formalism it describes the current division into n contacts in terms of the mutual conductance coefficients G_{ij} between the contacts. In this model, chiral current flow corresponds to the specific values of conductance coefficients given by Eq. (3). A non-chiral behavior would correspond to different values, including ad-

ditional non-zero conductance coefficients in Eq. (3). These would inevitably result in different plateau values of the predicted current ratios.

In all our measurements including three or four terminals shown in Fig. 5, Fig. 7 and Fig. 8, we instead see a perfect agreement between our chiral model prediction and the measured plateau values of the current ratios. This is in particular evident when comparing the horizontal dotted lines in Fig. 5(b) and Fig. 8, which indicate the predictions of Eq. (4) for the corresponding integer filling factors, with the corresponding measured plateau values.

This result stands in contrast to our finding in between plateaus, where the deviations of our measured currents from the prediction of Eq. (7) for $\mu B \gg 1$ provide a proof of non-chiral currents.

IV. SUMMARY AND OUTLOOK

We have performed multiterminal current measurements of a Hall bar in the regime of the QHE. We find that the current flow is chiral in the magnetic field regions of the quantized Hall resistance plateaus but becomes non-chiral in between the plateaus. Our result is based on the direct comparison of the measured current distribution into various contacts (three or four terminals) with two limiting models, which offer well understood, unique physical meanings. The classical Drude model serves us as the basis to describe non-chiral diffusive transport, while our second model is based on the generic chiral and coherent transmission problem. The comparison of different contact configurations for more than three terminals allows for a direct experimental proof of non-chiral currents, which confirm our model based results. Our work contributes to the understanding of the current flow inside mesoscopic devices in the regime of the QHE. It thereby confirms the assumption of chiral current flow frequently used for the case of quantized plateaus of the Hall resistance.

ACKNOWLEDGEMENT

The authors thank Piet Brouwer for help with the coherent model and Afif Siddiki for fruitful discussions. This work was funded by the Deutsche Forschungsgemeinschaft (DFG, German Research Foundation) – 218453298.

CONTRIBUTIONS OF THE AUTHORS

V. Y. U. supplied the wafer. S. S. and M. K. performed the measurements. S. S. and S. L. analyzed the data. S. L. derived the models. S. S. and S. L. wrote the article.

REFERENCES

-
- [1] M. Büttiker, Four-terminal phase-coherent conductance, *Phys. Rev. Lett.* **57**, 1761 (1986).
- [2] M. Büttiker, Absence of backscattering in the quantum Hall effect in multiprobe conductors, *Phys. Rev. B* **38**, 9375 (1988).
- [3] D. B. Chklovskii, B. I. Shklovskii, and L. I. Glazman, Electrostatics of edge channels, *Phys. Rev. B* **46**, 4026 (1992).
- [4] D. B. Chklovskii, K. A. Matveev, and B. I. Shklovskii, Ballistic conductance of interacting electrons in the quantum Hall regime, *Phys. Rev. B* **47**, 12605 (1993).
- [5] M. M. Fogler and B. I. Shklovskii, Resistance of a long wire in the quantum Hall regime, *Phys. Rev. B* **50**, 1656 (1994).
- [6] K. Lier and R. R. Gerhardt, Self-consistent calculations of edge channels in laterally confined two-dimensional electron systems, *Phys. Rev. B* **50**, 7757 (1994).
- [7] A. Siddiki and R. R. Gerhardt, Thomas-fermi-poisson theory of screening for laterally confined and unconfined two-dimensional electron systems in strong magnetic fields, *Phys. Rev. B* **68**, 125315 (2003).
- [8] A. Siddiki and R. R. Gerhardt, Incompressible strips in dissipative Hall bars as origin of quantized Hall plateaus, *Phys. Rev. B* **70**, 195335 (2004).
- [9] R. R. Gerhardt, The effect of screening on current distribution and conductance quantisation in narrow quantum Hall systems, *physica status solidi (b)* **245**, 378 (2008), <https://onlinelibrary.wiley.com/doi/pdf/10.1002/pssb.200743344>.
- [10] P. Armagnat and X. Waintal, Reconciling edge states with compressible stripes in a ballistic mesoscopic conductor, *Journal of Physics: Materials* **3**, 02LT01 (2020).
- [11] P. Weitz, E. Ahlswede, J. Weis, K. Klitzing, and K. Eberl, Hall-potential investigations under quantum Hall conditions using scanning force microscopy, *Physica E: Low-dimensional Systems and Nanostructures* **6**, 247 (2000).
- [12] E. Ahlswede, P. Weitz, J. Weis, K. von Klitzing, and K. Eberl, Hall potential profiles in the quantum Hall regime measured by a scanning force microscope, *Physica B: Condensed Matter* **298**, 562 (2001), international Conference on High Magnetic Fields in Semiconductors.
- [13] E. Ahlswede, J. Weis, K. v. Klitzing, and K. Eberl, Hall potential distribution in the quantum Hall regime in the vicinity of a potential probe contact, *Physica E: Low-dimensional Systems and Nanostructures* **12**, 165–168 (2002), proceedings of the Fourteenth International Conference on the Electronic Properties of Two-Dimensional Systems.
- [14] K. Güven and R. R. Gerhardt, Self-consistent local equilibrium model for density profile and distribution of dissipative currents in a hall bar under strong magnetic fields, *Phys. Rev. B* **67**, 115327 (2003).
- [15] S. Sirt and S. Ludwig, Current density distribution in the quantum hall effect (2024), [arXiv:2410.07943 \[cond-mat.mes-hall\]](https://arxiv.org/abs/2410.07943).
- [16] S. Sirt, V. Y. Umansky, A. Siddiki, and S. Ludwig, Direct measurement of bulk currents in the quantized hall regime (2024), [arXiv:2405.05138 \[cond-mat.mes-hall\]](https://arxiv.org/abs/2405.05138).
- [17] The slight deviations between the two are likely related with local changes in the sample during thermal cycles of the He-3 evaporation cryostat to $T > 4$ K between the two measurements.